PHYSICAL REVIEW C VOLUME 43, NUMBER 5 MAY 1991

Semiclassical distorted wave model of nucleon inelastic scattering to continuum

Y. L. Luo and M. Kawai
Department of Physics, Kyushu University 33, Fukuoka 812, Japan
(Received 17 September 1990)

A semiclassical distorted wave model is presented for one-step nucleon inelastic-scattering process leading to the continuous states of residual nucleus. The model is based on semiclassical approximations for the distorted waves and the Thomas-Fermi model of the nuclear states. The squared modulus of the matrix elements of nucleon-nucleon (N-N) interaction is substituted by the corresponding N-N scattering cross section in the free space. The model gives a closed-form expression with no adjustable free parameter for the double-differential cross section. We apply the model to the proton inelastic scattering from ^{120}Sn, ^{197}Au, and ^{209}Bi at 62 MeV, and ^{58}Ni at 100 and 164 MeV. Experimental data are reproduced very well at high emission energies except in small- and large-angle regions. The cross sections of the neutron inelastic scattering from ^{90}Zr, ^{120}Sn, and ^{208}Pb at 60 and 160 MeV, for which no experimental data are available, are predicted to be quite similar to the cross sections of the proton inelastic scattering. Calculations are also compared with the exciton model and the multistep direct reaction theory.

I. INTRODUCTION

Preequilibrium processes of nuclear reactions have been extensively studied since the 1960's. Various semiclassical[1] and quantal[2–4] methods have been proposed and used to analyze experimental data, and their theoretical foundations have been investigated.[5] It has been established by now that one can distinguish two mechanisms which contribute incoherently to the cross section:[2,5] The multistep direct (MSD) process and the multistep compound (MSC) process. Previous analyses have shown that MSD predominates in the high-energy part of the energy spectrum of emitted particles, and one- and two-step processes are the most important reaction mechanism there.[4,6]

The noncompound nucleus process was actually found in the late 1940's. Serber[7] pointed out that at high energies the first step in the reaction process could be regarded as collisions of the incident particle with individual nucleons in the nucleus whose binding could be neglected during the short time of the collision. Based on Serber's picture, Goldberger[8] proposed what is now called the intranuclear cascade model for nucleon-induced reactions.

A basic assumption of the cascade model is that the collisions at different points of the nucleus do not interfere with each other. Actually, the entire reaction process is a quantum-mechanical one. The assumption amounts to nucleon-nucleon collisions being spatially localized in the sense that outgoing waves emitted at different points of the nucleus do not interfere with each other.

In a previous paper,[9] hereafter referred to as I, we have shown that this assumption can be verified, within the framework of the distorted-wave Born approximation (DWBA), for the inclusive double-differential cross section of inelastic nucleon scattering, $(p,p'x)$ and $(n,n'x)$. The interference of the outgoing waves generated at different points of the nucleus is canceled out when the cross section is summed over a large number of nearly degenerate, mutually uncorrelated final states of the nucleus. A formula is derived for the double-differential cross section which manifestly expresses this and automatically incorporates the effect of distorting potentials, refraction, and absorption of the incident and outgoing fluxes. As in the cascade model, it has no adjustable parameter if one uses a free nucleon-nucleon scattering cross section in evaluating the local average two-nucleon cross section, in the spirit of impulse approximation, and nucleon optical potentials for the distorting potentials.

There is, however, one defect of the theory: the use of the geometrical optics approximation to the distorted waves. This approximation gives overall features of density and flux distributions, but not in detail. For example, it gives zero amplitude in the classically inaccessible region of space since it traces classical orbits. Also, actual calculations with this approximation are extremely cumbersome and have never been done.

In the present paper we extend the model of I to get rid of the geometrical optics approximation and make use of quantal distorted waves, though still with a semiclassical approximation, and allow for the finite, albeit short, range of nucleon-nucleon interaction which was neglected in I. We derive a formula for the double-differential cross section which has exactly the same appearance as the one derived in I. We apply the model to inclusive nucleon inelastic scattering on several target nuclei at energies up to about 200 MeV. A brief report of the calculations has been given in Ref. 10.

We present the results for (p,p') from ^{120}Sn, ^{197}Au, and ^{209}Bi at 62 MeV, and that from ^{58}Ni at 100 and 164 MeV. Nucleon optical potentials are used for the distorting potentials. The free nucleon-nucleon collision cross section averaged over the Fermi distribution of the target nucleons, with the Pauli principle taken into account,[11] is used for the calculation of the local average cross section. Thus there is no free adjustable parameter in the calcula-

tion. The experimental data are reproduced by the model very well at high emission energies except at very small and large angles. We also carry out calculations for (n,n'), even though there is no experimental data available at present. The cross sections show similar behavior as those for the proton.

In Sec. II, the formulation of the model is described. Numerical results of the calculations and comparison with experimental data are presented in Sec. III. In the last section a summary of the work is given, and discussions are given on the validity and limitations of the model, comparison with the exciton model, and previous quantal distorted-wave models.

II. FORMULATION

Our model starts from the DWBA expression of the double-differential inclusive cross section of nucleon inelastic scattering to continuum:

$$\frac{\partial^2\sigma}{\partial\varepsilon_f\partial\Omega_f}=\frac{1}{2}\sum_{s_i}\sum_{s_f}\frac{\mu^2}{(2\pi\hbar^2)^2}\frac{k_f}{k_i}\times\sum_f|\langle\hat{\chi}_f^{(-)}\Psi_f|V|\Psi_i\hat{\chi}_i^{(+)}\rangle|^2\times\delta(E_f-E_i)\ , \tag{2.1}$$

where μ is the reduced mass, k are the wave numbers, E are the total energies, Ψ are the nuclear wave functions, and χ are the distorted waves of the nucleon. The subscripts i and f stand for the initial and final states, respectively. We denote the energy and direction of emission by ε_f and Ω_f, respectively, and the incident energy by ε_i. The cross section is an average over the projectile spin directions s_i and a sum over the ejectile spin directions s_f and all the final nuclear states f. The delta function ensures the energy conservation. The potential V is a sum of two-body interaction potentials, $V=\sum_j v(\mathbf{r}_0,\mathbf{r}_j)$, between the incident nucleon and the nucleon in the target nucleus, with coordinate $\mathbf{r}_0$ for the incident nucleon and $\mathbf{r}_j$ for the jth target nucleon.

Further approximations are necessary for calculating the right-hand side (rhs) of Eq. (2.1) because of the large number and great complexity of the final nuclear states. Among the approximations proposed so far is the semiclassical model of I, based on the Thomas-Fermi model of the nuclear states, zero-range approximation for v, and geometrical optics approximation for the χ. We extend the model to allow for the finite range of v and to make use of quantal distorted waves, though still under a semiclassical approximation.

We assume, as in I, the single-particle model of the nucleus. We neglect antisymmetrization, which is presumably a reasonable approximation unless the incident energy is too low. The potential $v(\mathbf{r}_0,\mathbf{r}_j)$ can excite a nucleon from an initial single-particle state $\hat{\phi}_\alpha$ at energy ε_α to a final one $\hat{\phi}_\beta$ at ε_β. The subscripts α and β stand for spatial, spin, and isospin quantum numbers.

For simplicity, we assume that V and the distorting potentials U_i and U_f are spin and isospin independent. Extension to the case of more general v is straightforward and is actually used in the calculations discussed in the later sections. Under these assumptions, the average over s_i and the sum over s_f give unity, and Eq. (2.1) reduces to

$$\frac{\partial^2\sigma}{\partial\varepsilon_f\partial\Omega_f}=\frac{\mu^2}{(2\pi\hbar^2)^2}\frac{k_f}{k_i}4\sum_\alpha\sum_\beta\left|\int d\mathbf{r}_0 d\mathbf{r}\,\chi_f^*\phi_\beta^* v(\mathbf{r}_0-\mathbf{r})\phi_\alpha\chi_i\right|^2\delta(\varepsilon_f+\varepsilon_\beta-\varepsilon_\alpha-\varepsilon_i)\ , \tag{2.2}$$

where the ϕ and χ are the spatial parts of the $\hat{\phi}$ and the $\hat{\chi}$, respectively, and α and β now stand for the spatial quantum numbers only. The summation over α (β) is over all the occupied (unoccupied) orbits in the nucleus ground state. The factor 4 stems from the number of spin and isospin directions of the target nucleon in the initial state.

On expanding the squared modulus of the matrix element and exchanging the order of the summation and the integration, one has

$$\frac{\partial^2\sigma}{\partial\varepsilon_f\partial\Omega_f}=\frac{4\mu^2}{(2\pi\hbar^2)^2}\frac{k_f}{k_i}\int d\mathbf{r}_0 d\mathbf{r}\,\chi_f^*(\mathbf{r}_0)v(\mathbf{r}_0-\mathbf{r})\chi_i(\mathbf{r}_0)\int d\mathbf{r}_0' d\mathbf{r}'\chi_f(\mathbf{r}_0')v(\mathbf{r}_0'-\mathbf{r}')\chi_i^*(\mathbf{r}_0')K(\mathbf{r},\mathbf{r}')\ , \tag{2.3}$$

where

$$K(\mathbf{r},\mathbf{r}')\equiv\sum_\alpha\phi_\alpha^*(\mathbf{r}')\phi_\alpha(\mathbf{r})\sum_\beta\phi_\beta^*(\mathbf{r})\phi_\beta(\mathbf{r}')\delta(\varepsilon_f+\varepsilon_\beta-\varepsilon_\alpha-\varepsilon_i)\ . \tag{2.4}$$

Now our basic assumption is that the nucleon density $\rho(\mathbf{r})$ of the target nucleus is a slowly varying function of $\mathbf{r}$. We assume that the local density degenerate Fermi-gas model—Thomas-Fermi model for short—for the nuclear states is valid for calculating K. Thus $\sum_\alpha\phi_\alpha^*(\mathbf{r}')\phi_\alpha(\mathbf{r})$ and $\sum_\beta\phi_\beta^*(\mathbf{r})\phi_\beta(\mathbf{r}')$ are approximated by

$$\sum_\alpha\phi_\alpha(\mathbf{r})\phi_\alpha(\mathbf{r}')^*\simeq\frac{1}{(2\pi)^3}\int_{k<k_F(\mathbf{r})}d\mathbf{k}\,e^{i\mathbf{k}\cdot(\mathbf{r}-\mathbf{r}')}\ , \tag{2.5}$$

$$\sum_\beta\phi_\beta(\mathbf{r})^*\phi_\beta(\mathbf{r}')\simeq\frac{1}{(2\pi)^3}\int_{k'>k_F(\mathbf{r})}d\mathbf{k}'e^{i\mathbf{k}'\cdot(\mathbf{r}'-\mathbf{r})}\ , \tag{2.6}$$

for $\mathbf{r}$ and $\mathbf{r}'$ within a small cell in which $\rho(\mathbf{r})$ may be regarded as constant. In (2.5) and (2.6), $\hbar k_F(\mathbf{r})$ is the local Fermi momentum which is related to $\rho(\mathbf{r})$ by

$$\rho(\mathbf{r})=4\frac{4\pi}{3}\frac{k_F^3(\mathbf{r})}{(2\pi)^3}\ , \tag{2.7}$$

where the factor 4 takes care of the spin and isospin degrees of freedom. One sees that $k_F(\mathbf{r})$ is even more slowly varying function of $\mathbf{r}$ than $\rho(\mathbf{r})$. The rhs's of (2.5) and (2.6) are appreciable only for $|\mathbf{r}-\mathbf{r}'|\ll 1/k_F(\mathbf{r})$. Inserting (2.5) and (2.6) into (2.4), one obtains K, which is a function of $\mathbf{x}\equiv\mathbf{r}'-\mathbf{r}$,

$$K(\mathbf{r},\mathbf{r}')\equiv K(\mathbf{x})=\frac{1}{(2\pi)^6}\int_{k<k_F(\mathbf{r})}d\mathbf{k}e^{i\mathbf{k}\cdot\mathbf{x}}\int_{k'>k_F(\mathbf{r})}d\mathbf{k}'e^{i\mathbf{k}'\cdot\mathbf{x}}\delta(\varepsilon_f+\varepsilon'-\varepsilon-\varepsilon_i), \tag{2.8}$$

where ε_α and ε_β are replaced by $\varepsilon=\hbar^2k^2/2\mu$ and $\varepsilon'=\hbar^2k'^2/2\mu$ in the manner described in I. The function $K(\mathbf{x})$ also is appreciable only for small x, as shown in Sec. IV.

The slow variation of $\rho(\mathbf{r})$ results in variation of the distorting potentials for $\hat{\chi}_c^{(\pm)}(\mathbf{r})$:

$$U_c(\mathbf{r})=V_c(\mathbf{r})\pm iW_c(\mathbf{r})\ ,$$

where $c=i$ and f, and $(\pm)$ corresponds to $(+)$ and $(-)$ on the $\hat{\chi}$. Then the change in the amplitude of $\hat{\chi}_c^{(\pm)}$ within the cell may be neglected. If we put $\chi_c(\mathbf{r})=A_c(\mathbf{r})e^{iS_c(\mathbf{r})}$, therefore,

$$\chi_c(\mathbf{r}')\simeq A_c(\mathbf{r})e^{iS_c(\mathbf{r})+i\nabla S_c(\mathbf{r})(\mathbf{r}'-\mathbf{r})}=\chi_c(\mathbf{r})e^{i\mathbf{k}_c(\mathbf{r})\cdot\mathbf{x}}\ , \tag{2.9}$$

where

$$\mathbf{k}_c(\mathbf{r})\equiv\nabla S_c(\mathbf{r})\simeq\nabla\chi_c(\mathbf{r})/\chi_c(\mathbf{r})\ . \tag{2.10}$$

In the semiclassical approximation, $S_c(\mathbf{r})$ is the action function, and $\hbar\mathbf{k}_c(\mathbf{r})$ is the local momentum. The local energy $\varepsilon_c(\mathbf{r})\equiv\hbar^2k_c(\mathbf{r})^2/2\mu$ then satisfies

$$\varepsilon_c(\mathbf{r})+U_{c,\text{eff}}(\mathbf{r})=\varepsilon_c\ , \tag{2.11}$$

where, as shown in I,

$$U_{c,\text{eff}}(r,k_c)=\frac{1}{2}\left\{\frac{\hbar^2k_c}{2\mu}+V_c(r)-\left[\left[\frac{\hbar^2k_c}{2\mu}-V_c(r)\right]^2+W_c^2(r)\right]^{1/2}\right\}\ . \tag{2.12}$$

We make use of approximations (2.9), (2.10), and (2.11), although we use quantal $\chi_c(\mathbf{r})$. The slow variation of $U_c(\mathbf{r})$ implies that $\mathbf{k}_c(\mathbf{r})$ is a slowly varying function of $\mathbf{r}$, and its derivative can be neglected.

The two-body potential $v(\mathbf{r}-\mathbf{r}_0)$ has a short range and the kernel $K(\mathbf{r},\mathbf{r}')$ is appreciable only for small $\mathbf{r}'-\mathbf{r}$. The integrand of (2.3) is appreciable therefore only when $\boldsymbol{\rho}\equiv\mathbf{r}-\mathbf{r}_0$, $\boldsymbol{\rho}'\equiv\mathbf{r}'-\mathbf{r}_0'$, and $\mathbf{r}-\mathbf{r}'=\boldsymbol{\rho}-\boldsymbol{\rho}'-\mathbf{s}$ are small, and consequently $\mathbf{s}=\mathbf{r}_0'-\mathbf{r}_0$ is small. Putting (2.8) and (2.9), with approximation $k_F(\mathbf{r})\simeq k_F(\mathbf{r}_0)$, into (2.3), changing the variables of integration to $\mathbf{r}_0$, $\mathbf{s}$, $\boldsymbol{\rho}$, and $\boldsymbol{\rho}'$, and exchanging the order of the $\mathbf{k}$ integrations and the integrations over the coordinates, one obtains

$$\begin{aligned}\frac{\partial^2\sigma}{\partial\varepsilon_f\partial\Omega_f}=\frac{4\mu^2}{(2\pi\hbar^2)^2}\frac{k_f}{k_i}\frac{1}{(2\pi)^3}\int d\mathbf{r}_0|\chi_f(\mathbf{r}_0)|^2|\chi_i(\mathbf{r}_0)|^2\\ \times\int_{k<k_F(\mathbf{r}_0)}d\mathbf{k}\int_{k'>k_F(\mathbf{r}_0)}d\mathbf{k}'\left|\int d\boldsymbol{\rho}\,v(\boldsymbol{\rho})e^{i\mathbf{q}\cdot\boldsymbol{\rho}}\right|^2\delta(\mathbf{k}_f(\mathbf{r}_0)+\mathbf{k}'-\mathbf{k}_i(\mathbf{r}_0)-\mathbf{k})\\ \times\delta(\varepsilon_f(\mathbf{r}_0)+\varepsilon'-\varepsilon_i(\mathbf{r}_0)-\varepsilon)\ ,\end{aligned} \tag{2.13}$$

where $\mathbf{q}=\mathbf{k}-\mathbf{k}'$, $\varepsilon_f(\mathbf{r}_0)=\hbar^2k_f^2(\mathbf{r}_0)/2\mu$, and $\varepsilon_i(\mathbf{r}_0)=\hbar^2k_i^2(\mathbf{r}_0)/2\mu$, and the assumption $U_i\approx U_f$ is used.

It is convenient to introduce the center of mass and the relative momenta of the two-nucleon system in the initial and the final states by $\hbar$ times $\mathbf{K}_i=\mathbf{k}_i(\mathbf{r}_0)+\mathbf{k}$ and $\boldsymbol{\kappa}=[\mathbf{k}_i(\mathbf{r}_0)-\mathbf{k}]/2$, and $\mathbf{K}_f(\mathbf{r}_0)+\mathbf{k}'$ and $\boldsymbol{\kappa}'=[\mathbf{k}_f(\mathbf{r}_0)-\mathbf{k}']/2$, respectively. Then the $\mathbf{k}$ delta function dictates $\mathbf{K}_f=\mathbf{K}_i$, for which

$$\mathbf{k}'=\mathbf{k}_i(\mathbf{r}_0)+\mathbf{k}-\mathbf{k}_f(\mathbf{r}_0),\quad \mathbf{q}=\mathbf{k}-\mathbf{k}'=\mathbf{k}_f(\mathbf{r}_0)-\mathbf{k}_i(\mathbf{r}_0)=\boldsymbol{\kappa}'-\boldsymbol{\kappa}\ , \tag{2.14}$$

and

$$\delta(\varepsilon_f(\mathbf{r}_0)+\varepsilon'-\varepsilon_i(\mathbf{r}_0)-\varepsilon)=\frac{\mu}{\hbar^2}\delta(\kappa'^2-\kappa^2)\ . \tag{2.15}$$

Then

$$\left[\frac{\partial\sigma}{\partial\Omega_{\kappa'}}\right]_{NN}=\frac{(m/2)^2}{(2\pi\hbar^2)^2}\left|\int d\boldsymbol{\rho}\,v(\boldsymbol{\rho})e^{-i\mathbf{q}\cdot\boldsymbol{\rho}}\right|^2 \tag{2.16}$$

is the Born approximation to the differential cross section of nucleon-nucleon scattering from initial relative momentum $\hbar\boldsymbol{\kappa}$ to final one $\hbar\boldsymbol{\kappa}'$. Using (2.14), (2.15), and (2.16) in (2.13), and performing the $\mathbf{k}$ integration, one obtains

$$\frac{\partial^2\sigma}{\partial\varepsilon_f\partial\Omega_f}=\left[\frac{A}{A+1}\right]^2\int d\mathbf{r}|\chi_i(\mathbf{r})|^2|\chi_f(\mathbf{r})|^2\frac{k_f/k_f(\mathbf{r})}{k_i/k_i(\mathbf{r})}\left[\frac{\partial^2\sigma}{\partial\varepsilon_f(\mathbf{r})\partial\Omega_f(\mathbf{r})}\right]_{\mathbf{r}}\rho(\mathbf{r}) , \tag{2.17}$$

where

$$\left[\frac{\partial^2\sigma}{\partial\varepsilon_f(\mathbf{r})\partial\Omega_f(\mathbf{r})}\right]_{\mathbf{r}}=\frac{4mk_f(\mathbf{r})}{\hbar^2k_i(\mathbf{r})(4\pi/3)k_F(\mathbf{r})^3}\int_{k<k_F(\mathbf{r})}d\mathbf{k}\left[\frac{\partial\sigma}{\partial\Omega_{\kappa'}}\right]_{NN}\delta(\kappa'^2-\kappa^2) \tag{2.18}$$

is the local average cross section of two-nucleon scattering defined in Ref. 11 for the outgoing nucleon emitted at an energy within the interval $\varepsilon_f(\mathbf{r})\sim\varepsilon_f(\mathbf{r})+d\varepsilon_f(\mathbf{r})$ into a solid angle $d\Omega_f(\mathbf{r})$ around $\Omega_f(\mathbf{r})$, which corresponds to energy $\varepsilon_f\sim\varepsilon_f+d\varepsilon_f$ and solid angle $d\Omega_f$ around Ω_f. In (2.18), $\boldsymbol{\kappa}'$ should be understood to be $\boldsymbol{\kappa}+\mathbf{k}_f(\mathbf{r})-\mathbf{k}_i(\mathbf{r})$. Equation (2.17) is the final expression of the double-differential cross section in our model.

It is easy to interpret (2.18) if one transforms it as

$$d\sigma=\frac{1}{v_i(\mathbf{r})(4\pi/3)k_F(\mathbf{r})^3}\int_{k<k_F(\mathbf{r})}d\mathbf{k}v_{\rm rel}\left[\frac{\partial\sigma}{\partial\Omega_{\kappa'}}\right]_{NN}d\Omega_{\kappa'} . \tag{2.19}$$

making use of

$$d\varepsilon_f(\mathbf{r})d\Omega_f(\mathbf{r})=[mk_f(\mathbf{r})/\hbar^2]^{-1}d\mathbf{k}_f(\mathbf{r}) ,$$

$d\mathbf{k}_f(\mathbf{r})=d\boldsymbol{\kappa}'$ for a fixed $\mathbf{K}_f$,

$$\delta(\kappa'^2-\kappa^2)d\boldsymbol{\kappa}'=\delta(\kappa'-\kappa)/2\kappa d\kappa'=(\kappa/2)d\Omega_{\kappa'} ,$$

and $\kappa/k_i(\mathbf{r})=\frac{1}{2}v_{\rm rel}/v_i(\mathbf{r})$, where $v_{\rm rel}$ is the velocity of the incident particle relative to the colliding nucleon, and $v_i(\mathbf{r})$ is that in the laboratory system, both at $\mathbf{r}$. The rhs of (2.19) is the probability of the two-nucleon scattering into solid angle $d\Omega_{\kappa'}$ in the two-nucleon center of mass system, averaged over the Fermi distribution of the target nucleons, taking care of the Pauli principle, divided by the initial velocity, i.e., the desired differential average cross section.

We use for $(d\sigma/d\Omega)_{NN}$ the cross section of N-N scattering in the free space. The integrations over $\mathbf{k}$ in (2.18) can be carried out analytically if we neglect the energy and angular dependence of $(d\sigma/d\Omega)_{NN}$, with the approximation

$$(d\sigma/d\Omega)_{NN}\simeq\sigma_T(\varepsilon_i(r))/4\pi , \tag{2.20}$$

where $\sigma_T(\varepsilon_i(r))$ is the total cross section of nucleon-nucleon scattering in the free space at two-nucleon system laboratory energy $\varepsilon_i(r)$. The result is[11]

$$\left[\frac{\partial^2\sigma}{\partial\varepsilon_f\partial\Omega_f}\right]_{\mathbf{r}}=\frac{3\sigma_T(\varepsilon_i(r))}{4\pi k_F^3(r)}\frac{m^2}{\hbar^2}\frac{k_f(\mathbf{r})}{k_i(\mathbf{r})}W , \tag{2.21}$$

where

$$W=[k_i^2(\mathbf{r})-k_f^2(\mathbf{r})]/q(\mathbf{r}) , \tag{2.22a}$$

for $k_F^2\geq Z_0^2$ and $k_F^2\geq[q(\mathbf{r})+Z_0]^2$, and

$$W=\{k_i^2(\mathbf{r})k_f^2(\mathbf{r})\sin^2\theta-q^2(r)[k_f^2(\mathbf{r})-k_F^2(\mathbf{r})]\}/q^3(\mathbf{r}) , \tag{2.22b}$$

for $k_F^2\geq Z_0^2$ and $k_F^2\leq[q(\mathbf{r})+Z_0]^2$, where $\mathbf{q}(\mathbf{r})=\mathbf{k}_f(\mathbf{r})-\mathbf{k}_i(\mathbf{r})$ is the local momentum transfer, and $\theta=\angle(\mathbf{k}_f(\mathbf{r}),\mathbf{k}_i(\mathbf{r}))$ is the local scattering angle. The quantity Z_0 is defined by

$$Z_0=[k_i^2(\mathbf{r})-k_f^2(\mathbf{r})-q^2(\mathbf{r})]/2q(\mathbf{r}) . \tag{2.23}$$

One can calculate θ as follows. According to (2.10), the flux of the particle at $\mathbf{r}$ is given by

$$\begin{aligned}\mathbf{J}_c(\mathbf{r})&=-i\hbar[\chi_c^*(\mathbf{r})\nabla\chi_c(\mathbf{r})-\chi_c(\mathbf{r})\nabla\chi_c^*(\mathbf{r})]\\&\simeq\frac{\hbar}{m}|\chi_c(\mathbf{r})|^2\mathbf{k}_c(\mathbf{r}).\end{aligned} \tag{2.24}$$

Hence

$$\cos\theta=\frac{\mathbf{k}_i(\mathbf{r})\cdot\mathbf{k}_f(\mathbf{r})}{k_i(\mathbf{r})\cdot k_f(\mathbf{r})}\simeq\frac{\mathbf{J}_i(\mathbf{r})\cdot\mathbf{J}_f(\mathbf{r})}{J_i(\mathbf{r})\cdot J_f(\mathbf{r})} . \tag{2.25}$$

One can calculate $\mathbf{J}_c(\mathbf{r})$ with quantal $\chi_c(\mathbf{r})$. The method of calculation of $[\partial^2\sigma/\partial\varepsilon_f(\mathbf{r})\partial\Omega_f(\mathbf{r})]_{\mathbf{r}}$ described above is superior to the classical calculations described in I since it takes account of contributions from the regions which are inaccessible to classical trajectories. Besides, it has a very convenient form for numerical work with a computer.

III. RESULTS

In this section we present some results of our calculations with the formulas described in the previous section. First, we give a brief account of the input data of the calculations. Then we present results for $(p,p'x)$ and compare it with the experimental data. Finally, we give predictions for the cross sections of $(n,n'x)$ for which no experimental data are available at present.

A. Input data of numerical calculations

1. Distorting potentials

We use three sets of global optical potentials for different regions of energies of the incident and outgoing nucleons. The global potential of Menet *et al.*[12] with standard Woods-Saxon form is used for energies up to 62 MeV. The optical potential of Walter and Guss[13] is used for energies between 62 and 80 MeV. The optical potential of Nadasen *et al.*[14] is used for energies between 80 and 180 MeV. Spin-orbit potentials are omitted in all cases.

2. Nucleon density

We use the Fermi distribution form $\rho(r) = \rho_0/[1+\exp(r-R_\rho)/a_\rho]$ for the nucleon density, with the parameters $R_\rho = r_\rho A^{1/3}$ with $r_\rho = 1.15$ fm and $a_\rho = 0.5$ fm.[15] The constant ρ_0 is determined through the normalization $A = \int \rho(r) d\mathbf{r}$.

3. Free N-N scattering cross section

We assume that the free N-N cross sections are isotropic[11] and are $1/4\pi$ times

$$\sigma_{pp}(E_i) = 34.10/\beta^2 - 82.20/\beta + 82.20 ,$$

$$\sigma_{np}(E_i) = 10.63/\beta^2 - 29.92/\beta + 42.90 ,$$

with $\beta = v/c = [2E_i/(mc^2)]^{1/2}$ for pp and np cross sections, respectively. The neutron-neutron cross section $\sigma_{nn}(E_i)$ is assumed to be equal to $\sigma_{pp}(E_i)$. It is convenient to define σ_T as A times the average free N-N cross section for the nucleus, which is given by

$$\sigma_T(E_i) = (A-Z)\sigma_{np}(E_i) + Z\sigma_{pp}(E_i) ,$$

for incident proton, and

$$\sigma_T(E_i) = Z\sigma_{np}(E_i) + (A-Z)\sigma_{nn}(E_i) ,$$

for incident neutron.

B. Comparison with experimental data on (p,p') from ^{120}Sn, ^{197}Au, and ^{209}Bi at 62 MeV, and from ^{58}Ni at 100 and 164 MeV

The calculated angular distributions of the emitted protons are compared with experimental data[16] at the incident energy $E_i = 62$ MeV. The energy spectra are calculated at $E_i = 100$ and 164 MeV and are compared with experimental data[17] at several scattering angles.

Figures 1 and 2 show the angular distribution of proton inelastic scattering from ^{120}Sn and ^{197}Au, respectively, at $E_i = 62$ MeV and the exit energies $E_f = 50$ and 40 MeV. One sees that our model, with no adjustable parameter, agrees with the experimental data very well in the middle angular region, although the calculation underestimates the cross section at very small and large angles. The results of the exciton model[18] are also plotted in the figures. Most probably the emission from three-exciton states is predominant at the high exit energies

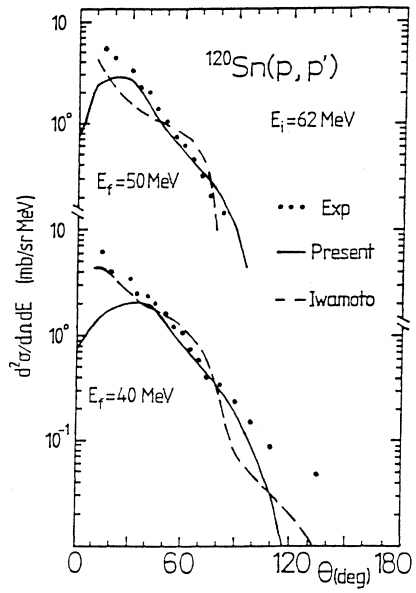

FIG. 1. Calculated and experimental angular distributions of ^{120}Sn(p,p') at $E_i = 62$ MeV for two different outgoing energies of 40 and 50 MeV. The solid lines represent the present calculation and the dashed lines that by Iwamoto and Harada (Ref. 18). The experimental data from Ref. 16 are indicated by the closed circles.

shown in the figures. This process may be regarded as corresponding to the one-step process of the present model as discussed in Sec. IV. The two models are in qualitative agreement with each other. More discussions on the comparison of the two models will be given in Sec. IV.

In Figs. 3 and 4, our results are also compared with the observed[16] angular distribution of protons in $(p,p'x)$ from

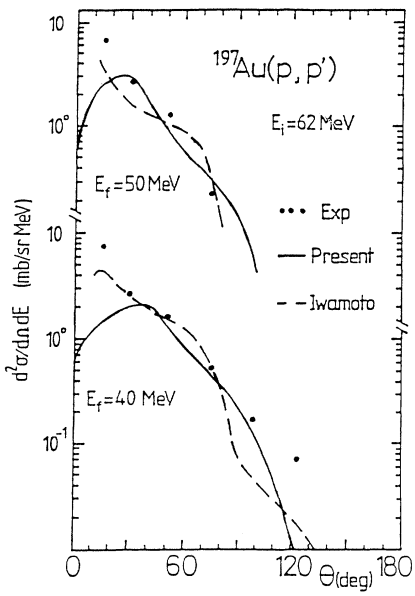

FIG. 2. Same as Fig. 1, but for ^{197}Au(p,p').

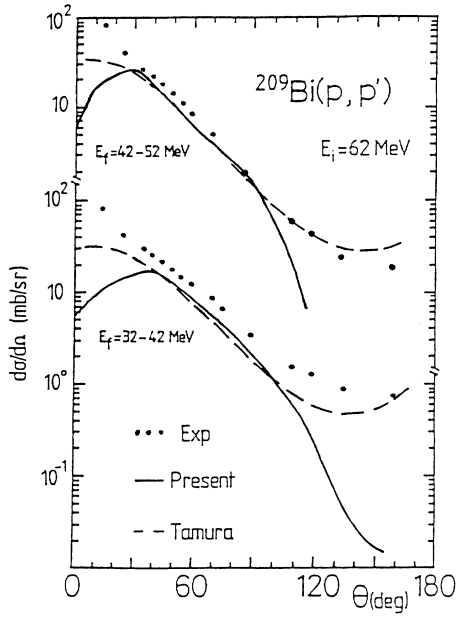

FIG. 3. Angular distribution of the cross sections summed over the 10-MeV energy bins of the emitted particles of ^{209}Bi(p,p') at $E_i=62$ MeV. The experimental data (closed circles) are from Ref. 16. The solid and dashed lines represent the present calculation and that by Tamura, Udagawa, and Lenske (Ref. 4), respectively.

^{209}Bi at $E_i=62$ MeV. The double-differential cross sections are integrated over the 10-MeV bins of the exit energy, between 42 and 52 MeV and 32 and 42 MeV in Fig. 3, and between 22 and 32 MeV in Fig. 4. Agreement with experimental data is good in the middle angular region at the high emission energies shown in Fig. 3. Disagreement with the experimental data at large angles

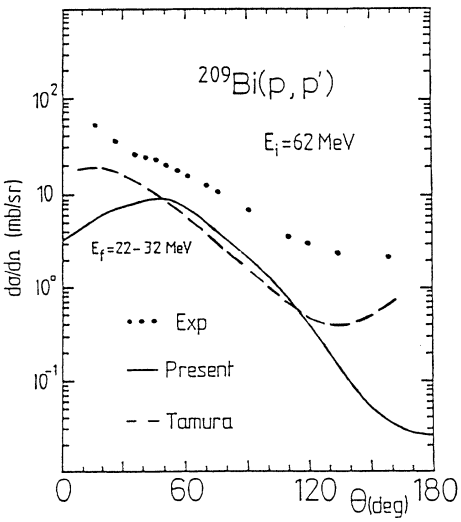

FIG. 4. Same as Fig. 3, but for $E_f=22-32$ MeV.

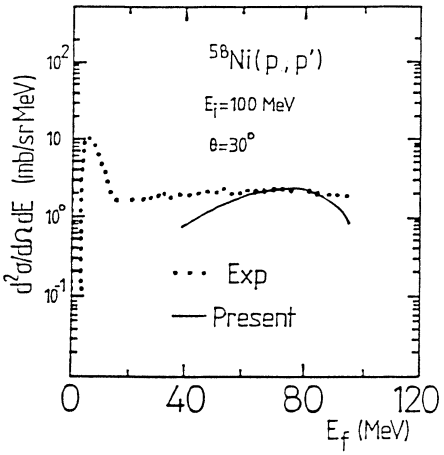

FIG. 5. Experimental and calculated proton energy spectra of ^{58}Ni(p,p') at $E_i=100$ MeV. The data are taken from Ref. 17. The solid line represents the present calculation.

and at the low emission energies shown in Fig. 4 is probably due to the contribution of multistep processes.

Comparison is also made with the one-step process part of the cross section calculated by Tamura, Udagawa, and Lenske.[4] The two models agree well with each other, although this depends on detailed assumptions used in Ref. 4 and on the assumptions made in our calculations as discussed in Sec. IV. The two models disagree at small and large angles, and at low energies. In the case of Fig. 4, Tamura, Udagawa, and Lenske estimate the contribution of two-step processes to be as much as 80% of the

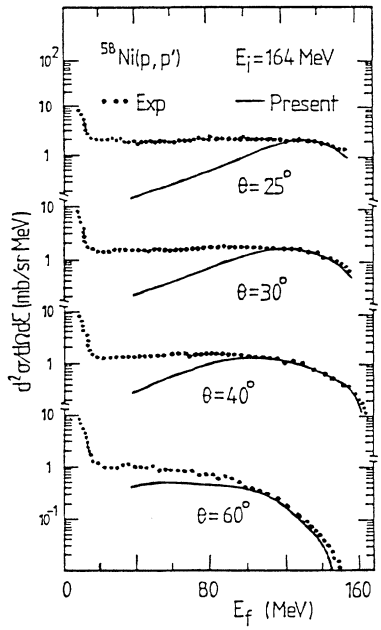

FIG. 6. Experimental and calculated proton energy spectra of ^{58}Ni(p,p') at $E_i=164$ MeV and emission angles 25°, 30°, 40°, and 60°. The data are taken from Ref. 17. Our results are denoted by the solid lines.

cross section.

The energy spectra are also calculated and compared with experimental data[17] at several exit angles. The results are shown in Figs. 5 and 6. Figure 5 shows the results for ^{58}Ni at $E_i = 100$ MeV and 30° of the exit angle. The result agrees with the experimental data very well at the emission energy E_f between about 60 and 85 MeV. At the lower E_f, the calculation underpredicts the experimental data. This is due partly to the neglect of higher-order processes. The results for the same target nucleus at $E_i = 164$ MeV and at the exit angles 25°, 30°, 40°, and 60° are shown in Fig. 6. At 40° excellent agreement between the calculation and experimental data is seen at E_f between about 100 and 155 MeV. The region of E_f in which the agreement is good narrows as the scattering angle deviates from 40°. This is in agreement with the trend in the angular distribution already mentioned; viz., the calculation well reproduces the experimental data in the middle angle region, but not at very small or large angles.

C. Predictions of neutron scattering cross sections of ^{90}Zr, ^{120}Sn, and ^{208}Pb at 60 and 160 MeV

Experimental data on (n,n') are unavailable in the energy region under consideration. We have calculated cross sections of (n,n') from ^{90}Zr, ^{120}Sn, and ^{208}Pb. Figures 7 and 8 show predictions of the angular distributions for ^{90}Zr and ^{208}Pb at $E_i = 60$ MeV and $E_f = 50$ MeV, and the energy spectra at $E_i = 160$ MeV and the exit angle 40°. The upper parts of the figures show, for comparison, the corresponding (p,p') cross section. One immediately sees that the (n,n') cross sections are very similar to the (p,p') ones, including their weak mass number dependence.

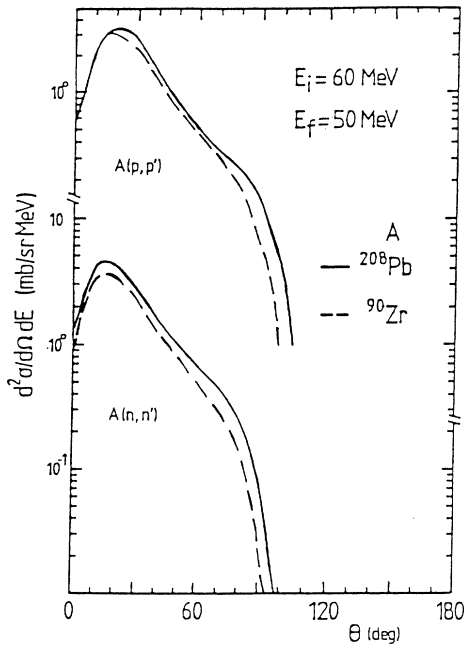

FIG. 7. Target mass number dependence of calculated nucleon angular distribution at $E_i = 60$ MeV and $E_f = 50$ MeV. The upper and lower parts correspond to (p,p') and (n,n'), respectively. The solid and dotted lines are for ^{208}Pb and ^{90}Zr, respectively.

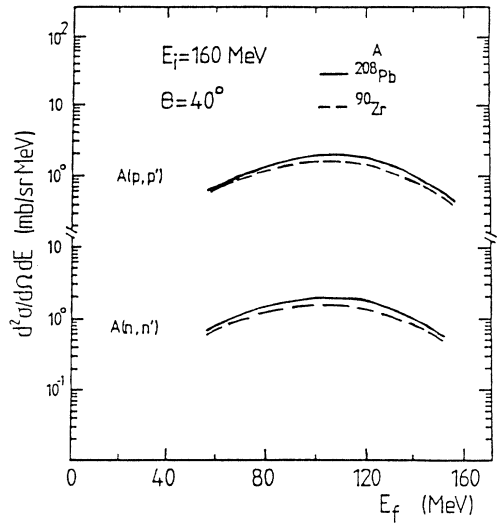

FIG. 8. Calculated energy spectra in (n,n') and (p,p') at $E_i = 160$ MeV and the emission angle 40°. The upper and lower parts correspond to (p,p') and (n,n'), respectively. The solid lines are for ^{208}Pb and the dashed lines for ^{90}Zr.

IV. SUMMARY AND DISCUSSIONS

A semiclassical distorted-wave theory based on the Thomas-Fermi model of the nucleus is presented for one-step nucleon inelastic scattering leading to continuous states of the residual nucleus. A simple closed-form expression [Eq. (2.17)] is derived for the double-differential inclusive cross section of inelastic scattering, (p,p',x) and $(n,n'x)$ and $(n,n'x)$, in terms of the average local nucleon-nucleon scattering cross section and nucleon density in individual cells of the nuclear medium, and the local fluxes of the incident and outgoing nucleons there. The formula justifies the concept of spatially localized nucleon-nucleon scattering in the nucleus, a basic assumption underlying all intranuclear cascade calculations.

The theory is applied to (p,p') on ^{58}Ni, ^{90}Zr, ^{120}Sn, ^{197}Au, ^{208}Pb, and ^{209}Bi at 60, 62, 100, 160, and 164 MeV. The calculated angular distribution from ^{120}Sn, ^{197}Au, and ^{209}Bi at 62 MeV is compared with experimental data. The calculation agrees with the data at high emission energies in the middle angular region. At small and large angles, the model underpredicts the cross section. As discussed later, this is a consequence of using the degenerate Fermi-gas model which strongly restricts the kinematical condition of scattering. Nonzero values of the calculated cross section in those angular regions are entirely due to the effect of distorting potentials. Energy spectra at fixed emission angles are also compared with experimental data for (p,p') on ^{58}Ni at 100 and 164 MeV.

At 40° the model reproduces the data at high emission energies, but underpredicts the cross section at low emission energies. This is consistent with the expectation that higher-order processes give large contributions there.

Predictions are made on the cross sections of (n,n') on ^{90}Zr, ^{120}Sn, and ^{208}Pb at 60 and 160 MeV at the emission angle 40°. The cross sections are similar to those of (p,p').

The model is compared with the exciton model (Ex) calculations of Ref. 18. Strictly speaking, emission from three-exciton states in Ex for an even-even target nucleus is different from the one-step process considered here: It includes processes via states of more excitons, and emission itself is treated as a statistical process satisfying the detailed balance. However, if, as in Ref. 18, the probability of going through higher exciton states is neglected ("never come back" assumption), the cross section is proportional to the one in the present model with constant nuclear density and without distorting potentials. The question then is how important is the effect of distorting potentials. Figure 9 shows the cross section of $(p,p'x)$ from ^{209}Bi at 62 MeV calculated with and without distorting potentials. The cross section with no distorting potentials vanishes at small and large angles. It is larger than the cross section with distortion by an order of magnitude. As a consequence, the exciton model cross sections have to be normalized by that much of a factor to be comparable with the ones of the present model, which agree in magnitude with experimental data without any renormalization.

The model is also compared with the multistep direct reaction (MSDR) model of Tamura, Udagawa, and Lenske[4] in which purely quantal DWBA cross sections for individual one-particle one-hole final states are calculated with collective form factors of appropriate strength, and summed over the energy range which corresponds to an energy interval in the spectrum of the emitted particle. The present model agrees well with the MSDR calculation of the cross sections at high energies and in middle angular regions where the present model is expected to be good. Agreement in the absolute magnitude of the cross sections should perhaps not be taken too seriously because of ambiguities in the models. At low emission energies, the agreement is not good, because of a two-step process which is not included in the present model. The reason for the discrepancy at large angles even at high emission energies is not clear for the moment.

Now we discuss some specific features of our calculations. The first point is how much the calculated cross sections depend on the choice of distorting potentials. Figure 10 shows the cross sections obtained with two different sets of global optical potentials, one given by Menet *et al.*[12] and the other given by Walter and Guss.[13] At $E_i=62$ MeV, the two sets give results which are almost identical at $E_f=50$ MeV, and only slightly different at small and large angles at $E_f=30$ MeV. Thus we conclude that, in the cases studied here, the dependence on the distorting potentials is negligible in the angular region in which our model is successful.

The second point is the range of kernel $K(x)$, defined by (2.8), on which the validity of approximation (2.9), for the distorted waves depends. Figure 11 shows $K(x)$ for $E_i=62$ MeV and $E_f=30$ MeV, and for Fermi energy $E_f\equiv\hbar^2k_F^2/2m=1.6$, 10.6, and 30.3 MeV, which correspond to the local Fermi energy of ^{197}Au at $r=9.0$, 7.5, and 6.0 fm. One sees that the range of the kernel remains

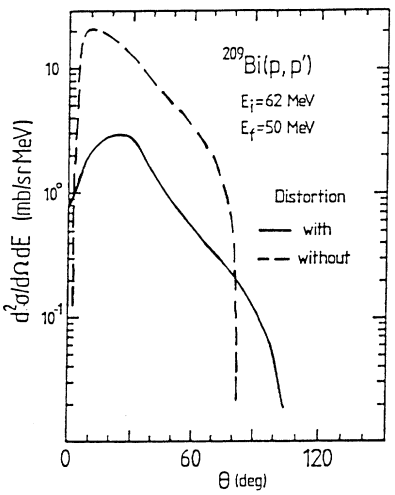

FIG. 9. Effect of distortion on the angular distribution of ^{209}Bi(p,p') at $E_i=62$ MeV and $E_f=50$ MeV. The solid and dashed lines represent the results of the calculations with and without the distorting potentials, respectively.

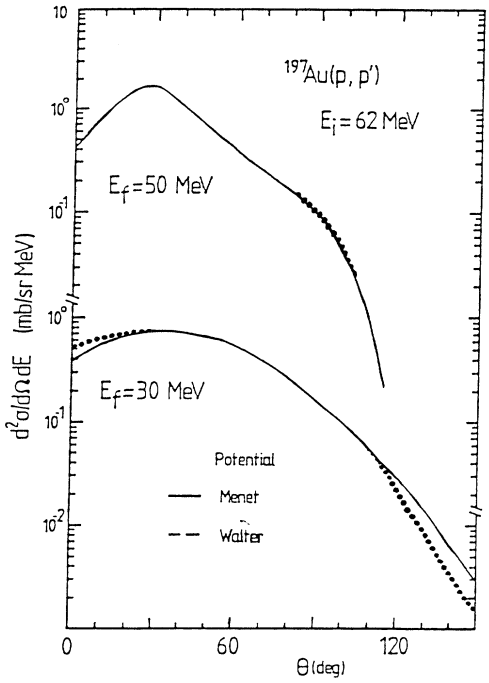

FIG. 10. Distorting potential dependence of calculated cross section for the cases of ^{197}Au(p,p') at $E_i=62$ MeV and $E_f=50$ and 30 MeV. The solid and dashed lines represent the results with the distorting potentials by Menet *et al.* (Ref. 12) and Walter and Guss (Ref. 13), respectively.

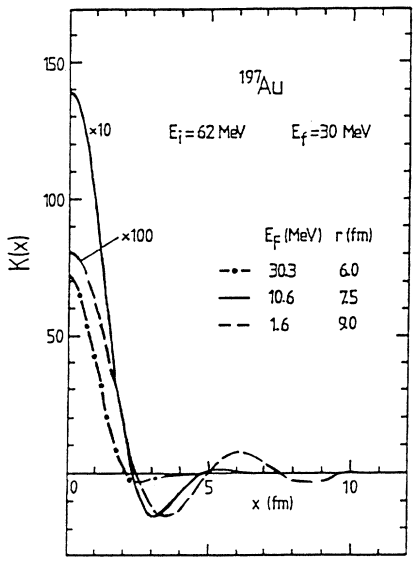

FIG. 11. Kernel at $E_i=62$ MeV and $E_f=30$ MeV for three values of the Fermi energies E_F, which correspond to the densities at three distances r from the center of the nucleus ^{197}Au.

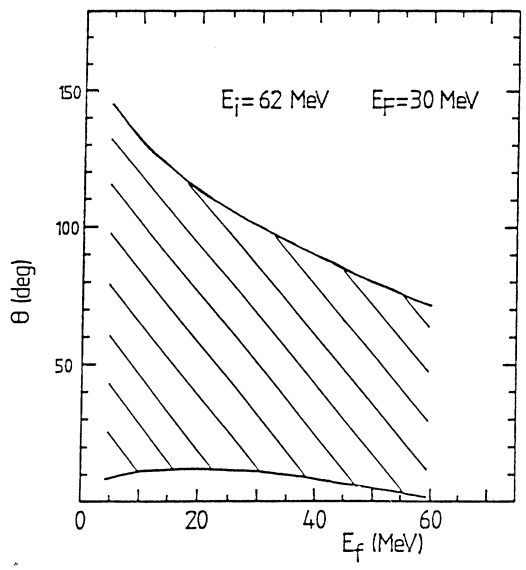

FIG. 12. Region of nonzero local average N-N cross section at $E_F=30$ MeV and $E_i=62$ MeV shown by the hatched area in the local-emission-energy–emission-angle diagram.

indeed small, close to about 1 fm, even though its maximum decreases as $E_F(\mathbf{r})$ decreases. This assures that approximation (2.9) is fairly good.

The third point is the reason why the model underestimates the cross section at small and large angles, as already mentioned. This may be understood qualitatively by the behavior of the local average scattering cross section $[\partial^2\sigma/\partial\varepsilon_f(\mathbf{r})\partial\Omega_f(\mathbf{r})]_r$. The hatched region in Fig. 12 represents the region of $\varepsilon_f(\mathbf{r})$ and $\theta_f(\mathbf{r})$ in which $[\partial^2\sigma/\partial\varepsilon_f(\mathbf{r})\partial\Omega_f(\mathbf{r})]_r$ is nonzero, in the case of $\varepsilon_i(\mathbf{r})=62$ MeV and $E_F(\mathbf{r})=30$ MeV as an example. At almost all $\varepsilon_f(\mathbf{r})$, the cross section is completely zero at small and large angles. This is because such scattering is kinematically forbidden by the Pauli principle in the degenerate Fermi-gas model. If there were no distorting potentials and no variation of the nuclear density, the angular distributions of the (p,p') cross section would be the same as $[\partial^2\sigma/\partial\varepsilon_f(\mathbf{r})\partial\Omega_f(\mathbf{r})]_r$. Distorting potentials deflect the motion of the incident and outgoing particles, and give rise to nonzero cross sections in the "forbidden" regions, but the cross section is still smaller there than in the "allowed" angular region. The allowed region gets narrower as the local emission energy increases.

It is very encouraging that the experimental data are reproduced well by the calculation in the energy and angular regions where the model is expected to work. Agreement in the absolute magnitude of the cross sections is significant since the model includes no adjustable parameter. It clearly shows the basic soundness of the model, although nearly perfect agreement at certain angles and energies should not be taken too seriously until justification is given of the use of the free nucleon-nucleon scattering cross section for a collision in the nuclear medium at the energies and angular regions investigated here. It seems worthwhile in any case to pursue refinements and extensions of the model and widen its range of applicability. For example, the free N-N cross section should be corrected for medium effects. The theory must be extended to include two-step processes which are important at low emission energies, sometimes even more so than the one-step process. Development in this direction is in progress and will be reported in later communications.

ACKNOWLEDGMENTS

The authors wish to thank Professor H. A. Weidenmüller and all members of the theoretical nuclear physics group at Kyushu University for their interest in this work and encouragement. They are indebted to Institute for Nuclear Study, University of Tokyo, for the financial aid of the computation which was done at the Computer Center of Kyushu University with the FACOM M780/VP200 computer.

[1]J. J. Griffin, Phys. Rev. Lett. **17**, 478 (1966); M. Blann, Annu. Rev. Nucl. Sci. **25**, 123 (1975); G. Mantzouranis, H. A. Weidenmüller, and D. Agassi, Z. Phys. A **276**, 145 (1976).

[2]H. Feshbach, A. Kerman, and S. Koonin, Ann. Phys. (N.Y.) **125**, 429 (1980).

[3]G. F. Bertsch and F. S. Tasi, Phys. Rep. C **18**, 125 (1975).

[4]T. Tamura, T. Udagawa, and H. Lenske, Phys. Rev. C **26**, 379 (1982).

[5]N. Nishioka, H. A. Weidenmüller, and S. Yoshida, Ann. Phys. (N.Y.) **183**, 166 (1988); **193**, 195 (1989).
[6]H. C. Chiang and J. Hüfner, Nucl. Phys. **A349**, 466 (1980).
[7]R. Serber, Phys. Rev. **72**, 1114 (1947).
[8]M. L. Goldberger, Phys. Rev. **74**, 1269 (1948).
[9]M. Kawai, Prog. Theor. Phys. **27**, 155 (1962).
[10]Y. L. Luo and M. Kawai, Phys. Lett. B **235**, 211 (1990).
[11]K. Kikuchi and M. Kawai, *Nuclear Matter and Nuclear Reactions* (North-Holland, Amsterdam, 1968), p. 33.
[12]J. J. H. Menet, E. E. Gross, J. J. Malanify, and A. Zucher, Phys. Rev. C **4**, 1114 (1971).
[13]R. L. Walter and P. P. Guss, in *Nuclear Data for Basic and Applied Science,* Proceedings of the International Conference, Santa Fe, New Mexico, 1985, edited by P. G. Young, R. E. Brown, G. F. Auchampaugh, P. W. Lisowski, and L. Stewart (Gordon and Breach, New York, 1986), Vol. 1, p. 1079.
[14]A. Nadasen, P. P. Singh, W. W. Jacobs, A. D. Bacher, P. T. Deber, M. D. Kailchuch, and J. T. Meek, Phys. Rev. C **23**, 1023 (1981).
[15]J. M. Pearson, *Nuclear Physics: Energy and Matter* (Hilger, London, 1986), p. 16.
[16]F. E. Bertrand and R. W. Peele, Phys. Rev. C **8**, 1045 (1973); Oak Ridge National Laboratory Report No. ORNL-4460, 1960; No. ORNL-4471 1970; No. ORNL-4638, 1971.
[17]R. E. Segel, T. Chen, L. L. Rutledge, J. V. Maher, J. Wiggins, P. P. Singh, and P. T. Debevec, Phys. Rev. C **26**, 2424 (1982).
[18]A. Iwamoto and K. Harada, Nucl. Phys. **A419**, 472 (1984).